Received: 26 September 2022 | Revised: 20 February 2023 | Accepted: 20 February 2023

DOI: 10.1002/mp.16355

RESEARCH ARTICLE

MEDICAL PHYSICS

Depth-of-interaction positron emission tomography detector with 45° tilted silicon photomultipliers using dual-ended signal readout

Minjee Seo[1,2] | **Haewook Park**[1,2] | **Seungeun Lee**[1,2] | **Guen Bae Ko**[3,4] | **Jae Sung Lee**[1,2,3,4]

[1]Department of Biomedical Sciences, Seoul National University College of Medicine, Seoul, South Korea

[2]Department of Nuclear Medicine, Seoul National University College of Medicine, Seoul, South Korea

[3]Institute of Radiation Medicine, Medical Research Center, Seoul National University College of Medicine, Seoul, South Korea

[4]Brightonix Imaging Inc., Seoul, South Korea

Correspondence
Jae Sung Lee, Department of Nuclear Medicine, Seoul National University College of Medicine, 103 Daehak-ro, Jongno-gu, Seoul 03080, South Korea.
Email: jaes@snu.ac.kr

Guen Bae Ko, Brightonix Imaging Inc., 25 Yeonmujang 5ga-gil, Seongdong-gu, Seoul 04782, South Korea.
Email: gbko@brtnx.com

Funding information
Korea Medical Device Development Fund (KMDF); Korean Ministry of Science and ICT, Ministry of Trade, Industry and Energy, Ministry of Health & Welfare, Ministry of Food and Drug Safety, Grant/Award Numbers: 1711137868, RS-2020-KD000006; National Research Foundation of Korea (NRF); Korean Ministry of Science and ICT, Grant/Award Number: 2020M2D9A1093989; National Research Foundation of Korea (NRF);

Abstract

Background: Small-animal positron emission tomography (PET) systems are widely used in molecular imaging research and drug development. There is also growing interest in organ-dedicated clinical PET systems. In these small-diameter PET systems, the measurement of the depth-of-interaction (DOI) of annihilation photons in scintillation crystals allows for the correction of parallax error in PET system, leading to an improvement on the spatial resolution uniformity. The DOI information is also useful for improving the timing resolution of PET system as it enables the correction of DOI-dependent time walk in the arrival time difference measurement of annihilation photon pairs. The dual-ended readout scheme is one of the most widely investigated DOI measurement methods, which collects visible photons using a pair of photosensors located at both ends of the scintillation crystal. Although the dual-ended readout allows for simple and accurate DOI estimation, it requires twice the number of photosensors compared to the single-ended readout scheme.

Purpose: To effectively reduce the number of photosensors in a dual-ended readout scheme, we propose a novel PET detector configuration that employs 45° tilted and sparsely arranged silicon photomultipliers (SiPMs). In this configuration, the angle between the scintillation crystal and SiPM is 45°. Therefore, and thus, the diagonal of the scintillation crystal matches one of the lateral sides of the SiPM. Accordingly, it allows for the use of SiPM device larger than the scintillation crystal, thereby improving light collection efficiency with a higher fill factor and reducing SiPM quantity. In addition, all scintillation crystals can achieve more uniform performance than other dual-ended readout methods with a sparse SiPM arrangement because 50% of the scintillation crystal cross section is commonly in contact with the SiPM.

Methods: To demonstrate the feasibility of our proposed concept, we implemented a PET detector that employs a 4×4 LSO block with a single crystal dimension of $3.03 \times 3.03 \times 20$ mm^3 and a 45° tilted SiPM array. The 45° tilted SiPM array consists of 2×3 SiPM elements at the top ("*Top SiPM*") and 3×2 SiPM elements at the bottom ("*Bottom SiPM*"). Each crystal element of the 4×4 LSO block is optically coupled with each quarter section of the *Top SiPM* and *Bottom SiPM* pair. To characterize the performance of the PET detector, the energy, DOI, and timing resolution were measured for

Minjee Seo and Haewook Park contributed equally to this work.

Ministry of Education, Grant/Award Number: 2018R1D1A1B07045559

all 16 crystals. The energy data was obtained by summing all the charges from the *Top SiPMs* and *Bottom SiPM*s, and the DOI resolution was measured by irradiating the side of the crystal block at five different depths (2, 6, 10, 14, and 18 mm). The timing was estimated by averaging the arrival time of the annihilation photons measured at the *Top SiPMs* and *Bottom SiPMs* (Method 1). The DOI-dependent time-walk effect was further corrected by using DOI information and statistical variations in the trigger times at the *Top SiPMs* and *Bottom SiPMs* (Method 2).
Results: The average DOI resolution of the proposed PET detector was 2.5 mm, thereby resolving the DOI at five different depths, and the average energy resolution was 16% full width at half maximum (FWHM). When Methods 1 and 2 were applied, the coincidence timing resolutions were 448 and 411 ps FWHM, respectively.
Conclusions: We expect that our novel low-cost PET detector design with 45° tilted SiPMs and a dual-ended readout scheme would be a suitable solution for constructing a high-resolution PET system with DOI encoding capability.

KEYWORDS
depth-of-interaction (DOI), dual-ended signal readout, high-resolution, positron emission tomography (PET), silicon photomultiplier (SiPM)

1 INTRODUCTION

Positron emission tomography (PET) is a useful tool for the non-invasive visualization of metabolic processes and molecular pathways in the living body.[1–3] Small-animal PET scanners are widely used in molecular imaging research and novel drug development.[4–6] In addition, there is growing interest in imaging single specific organs, such as the brain and breast, using organ-dedicated PET scanners with high spatial resolution and sensitivity.[7–13] Organ-dedicated PET scanners are also useful in terms of footprint size and patient throughput.

However, the small diameter of small-animal and organ-dedicated PET scanners causes parallax errors, thereby degrading the spatial resolution uniformity. Parallax errors can be overcome by locating the exact interaction position of 511-keV annihilation photons within the scintillation crystal, as known as the depth-of-interaction (DOI) information.[14] DOI information is also useful for improving the timing resolution of PET detectors by correcting the DOI-dependent time walk that occurs during the arrival-time measurement of incoming scintillation photons.[15,16] Therefore, various DOI measurement methods based on single-ended and dual-ended readout schemes have been investigated. The single-ended readout methods include discrete DOI measurements, such as phoswich detector and multi-layer crystal design,[17–20] and continuous DOI measurements, such as modified reflector design, light sharing method, and using monolithic crystal.[21–23]

Thanks to the accurate DOI estimation and simplicity in DOI calibration, the dual-ended readout method is one of the most intensively investigated approaches.[24–31] However, it requires twice as many photosensors and electronics compared to other DOI measurement methods[14,32–35] based on a single-ended signal readout. Therefore, cost-effective PET detectors based on sparsely arranged photosensor configurations have been proposed to reduce detector manufacturing costs for the dual-ended readout method.[28,29]

In this study, we propose and validate a novel PET detector configuration that utilizes 45° tilted and sparsely arranged silicon photomultiplier (SiPM) elements, which is potentially useful for cost-effective dual-ended signal readout (Figure 1a). In our proposed method, the angle between the scintillation crystal and SiPM is 45°. Therefore, 50% of the crystal cross-section is commonly in contact with the photosensor, allowing for uniform performance across all the scintillation crystals. In comparison with the dichotomous offset quadrant-sharing design (DO-QS),[28] one of the previous dual-ended readout methods based on sparse SiPM arrangement (Figure 1b), our method reduces scintillation light loss by using larger photosensors (Table 1). Although DO-QS can achieve uniform light collection performance for each crystal, only 25% of the crystal cross-section is in contact with the SiPMs (Figure 1b). The dual-sided position-sensitive sparse sensor (DS-PS3),[29] which is another sparse SiPM configuration for dual-ended readout (Figure 1c), features higher sparsity than our 45° tilted method. However, our proposed method has an advantage over DS-PS3 in terms of light collection efficiency.

This paper is structured as follows. First, we introduce the proposed detector configuration and front-end electronics in detail. Second, the detailed data acquisition

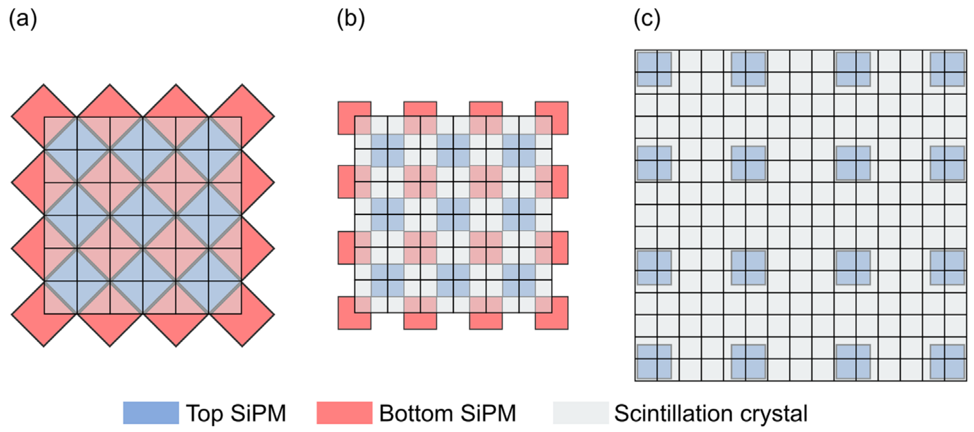

FIGURE 1 Dual-ended readout schemes based on a sparse SiPM arrangement. (a) 45° tilted SiPMs (proposed method), (b) Dichotomous Offset Quadrant-Sharing detector design (DO-QS),[28] and (c) Dual-Sided Position-Sensitive Sparse-Sensor (DS-PS3) detector (*Top SiPM* and *Bottom SiPM* are overlapped in the same position).[29]

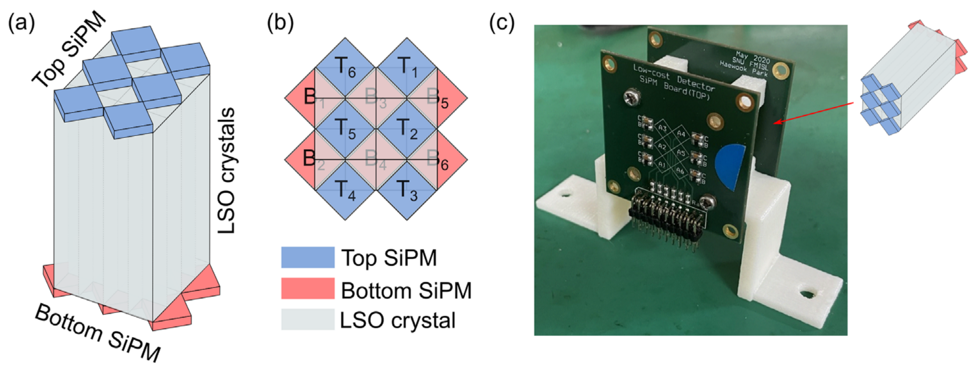

FIGURE 2 PET detector configuration with sparse SiPM arrangement: (a) 3D view, (b) 2D map of the *Top SiPMs* and *Bottom SiPMs*, and (c) experimental setup on an in-house built printed circuit board.

TABLE 1 Comparison of various dual-ended readout schemes.

	45°s tilted	DO-QS	DS-PS3
# of crystal	$2n \times 2n$	$2n \times 2n$	15×15
# of SiPM	$2n^2 + 2n + 1$	$2n^2 + 2n + 1$	$4 \times 4 \times 2$
Size of crystal (mm^2)	$a \times a$	$a \times a$	1.917×1.917
Size of SiPM (mm^2)	$\sqrt{2}a \times \sqrt{2}a$	$a \times a$	3×3

setup and analysis method for evaluating the proposed method are described. Last, the detector performances, including the DOI, energy, and timing resolutions, are provided and discussed.

2 | MATERIALS AND METHODS

2.1 | PET detector configuration

To demonstrate the feasibility of our method, we developed a PET detector using a 4 × 4 LSO block and 45° tilted SiPM array, as shown in Figure 2. The 45° tilted SiPM array consists of a 2 × 3 SiPM element at the top ("*Top SiPM*") and a 3 × 2 SiPM element at the bottom ("*Bottom SiPM*"). Twelve single-channel SiPMs (S14160-4050HS; Hamamatsu Photonics K. K., Japan) were used for the *Top SiPM* and *Bottom SiPM* assemblies, and a 4 × 4 LSO block (Sichuan Tianle Photonics, China) was used. The dimension of the single LSO crystal element was $3.03 \times 3.03 \times 20$ mm^3. Each LSO crystal was coupled with quarters of the *Top SiPM* and *Bottom SiPM* pair (one above and one below) via silicon grease (BC-630; Saint-Gobain Crystals, France). The diagonal length of each scintillation crystal surface at the entrance side is the same as the pitch of SiPM. The lateral sides of all 16 LSO crystals were roughened (500 grit) to enable DOI encoding, and the entrance sides of all LSO crystals were polished to improve light collection efficiency.[25,31] All LSO crystals were optically isolated using $BaSO_4$ diffusive reflectors to achieve better DOI resolution.[36]

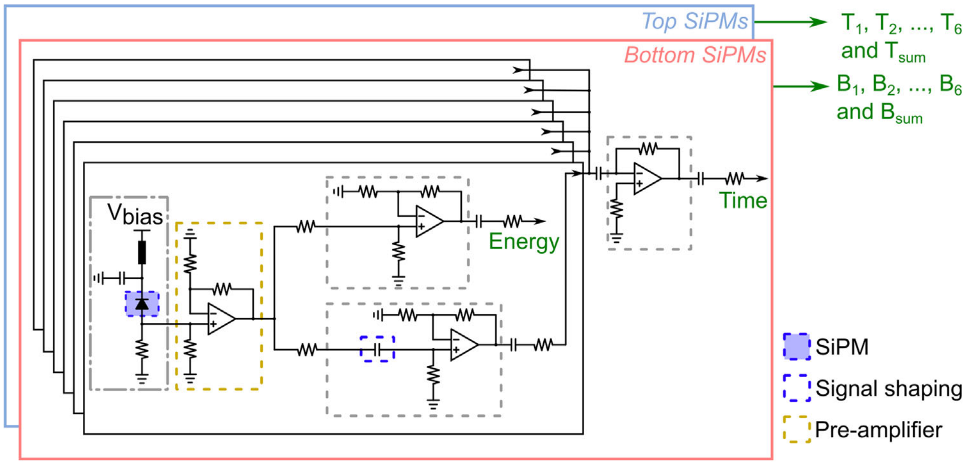

FIGURE 3 Schematic of front-end electronics.

2.2 | Front-end electronics

Figure 3 shows the schematic of front-end electronics on an in-house built printed circuit board used in this study. A bias voltage (V_{bias}) was applied to each SiPM via the cathode. Each SiPM anode signal was divided into two branches after being amplified by a non-inverting pre-amplifier. One branched signal was amplified using a non-inverting amplifier to generate an energy signal while the other branched signal was passed through a first-order capacitive filter to enhance the timing performance. The filtered signals were amplified using non-inverting amplifiers and subsequently summed to generate time signals. The energy signals of the *Top SiPM* and *Bottom SiPM* are labeled as T_1, T_2, …, and T_6 and B_1, B_2, …, and B_6, respectively. The time signals of the *Top SiPM* and *Bottom SiPM* are denoted as T_{sum} and B_{sum}, respectively.

2.3 | Experimental setup

Figure 4 illustrates the experimental setup. For side-on irradiation, we used a reference detector based on a Hamamatsu R9800 photomultiplier tube (PMT) coupled with a 1 × 13 × 20 mm^3 single LSO slab to achieve electronic collimation with a 1.2-mm wide beam irradiation.[32] The proposed PET detector was placed on a 1-axis linear translation stage and irradiated at various axial positions of 2, 6, 10, 14, and 18 mm from the *Top SiPM* (Figure 4a) using a ^{22}Na point source (~5.11 μCi). For head-on irradiation, another reference detector consisting of an R9800 PMT and 3 × 3 × 3 mm^3 LSO crystal was used. Another ^{22}Na source (~6.63 μCi) was placed between the reference and proposed PET detectors. The single timing resolution (STR) of the reference detector used for head-on irradiation was 197 ps full width at half maximum (FWHM). All measurements were performed in a thermostatic chamber at 20°C.

Nuclear instrumentation modules (NIMs) were employed for coincidence detection. The PMT anode signal (*Ref*) and time signals of the *Top SiPM* and *Bottom SiPMs* (T_{sum} and B_{sum}) were duplicated using a fan-in/fan-out NIM (N401; CAEN, Italy) and fed into a NIM constant fraction discriminator (N843; CAEN, Italy) to generate trigger signals. The trigger signals from the proposed PET detector and reference detector were fed into a NIM AND logic gate (N405, CAEN) and subsequently connected to a fast-trigger port (TR0) as an input for a 16+1 channel domino-ring sampler 4 (DRS4)-based digitizer (DT5742B; CAEN, Italy) that has a 12-bit analog-to-digital converter (ADC). The PMT anode signal, energy signals of the *Top SiPM* and *Bottom SiPM*, and time signals were individually sampled by the DRS4 digitizer with a sampling rate of 5 Giga samples per second (GSPS).

2.4 | Data analysis

Due to the dispersion of scintillation light, each SiPM element within the 45° tilted SiPM array can detect scintillation light not only from the directly coupled crystals but also from other surrounding crystals. Therefore, two valid energy signals must be carefully selected from the 12 energy signals for each annihilation event. The crystal identification procedure is as follows. First, we integrated the charge of each energy signal of the *Top SiPM* and *Bottom SiPM* with an integration window of 120 ns. Second, the SiPM element with the maximum integration charge among each of the *Top SiPM* and *Bottom SiPM* was identified, which was denoted as the “*active Top SiPM*” and “*active bottom SiPM*”, respectively. Last, the interacting crystal element was looked up from the 16 combinations of the *Active*

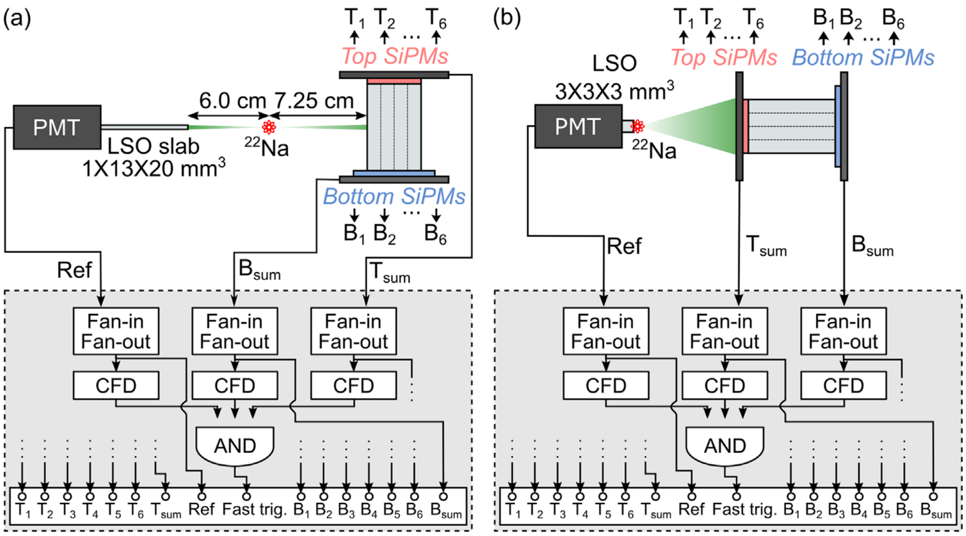

FIGURE 4 Experimental setup: (a) side-on irradiation and (b) head-on irradiation.

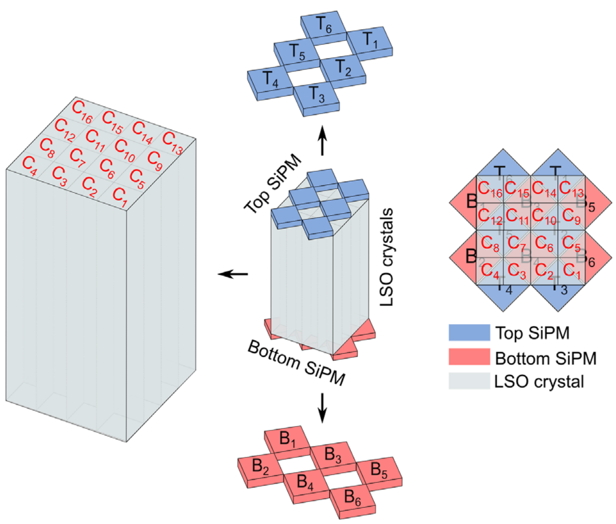

FIGURE 5 Illustration for look-up-table. C_n is each of the LSO crystal elements in our detector (n = 1, 2, …, 16). For example, if *Active Top SiPM* and *Active Bottom SiPM* are T_2 and B_4 then the interacted crystal is C_6.

Top SiPM and *Active Bottom SiPM*, as illustrated in Figure 5.

The deposited energy of the proposed PET detector was calculated by summing all the integrated charges of the *Top SiPM* and *Bottom SiPM*. The energy resolution was calculated as a percentage by dividing the FWHM value by the 511-keV photopeak value from the deposited energy histogram. We did not correct for SiPM saturation effects in this study.

The DOI index was calculated as follows:

$$\text{DOI index} = \frac{C_T - C_B}{C_T + C_B} \tag{1}$$

where C_T and C_B are the integrated charges on the *Top SiPM* and *Bottom SiPM*, respectively. After fitting the DOI spectrum using a Gaussian curve at each depth position, the DOI resolution was calculated by averaging the FWHM of each DOI index distribution. The DOI indices were converted to the vertical position in the scintillation crystal (see Figure 4a) according to the linear relationships between the five irradiation depths (mm) and peak positions in the DOI histogram (DOI index).[37,38]

The arrival time was determined using two different methods to correct the DOI-dependent time walk owing to annihilation and optical photon travel within the scintillation crystal.[15] In Method 1, the triggered time (also called the timestamp, *TS*) of the proposed PET detector was calculated by averaging the timestamps from the *Top SiPM* and *Bottom SiPM* as follows:

$$TS_{det} = \frac{TS_T + TS_B}{2} \tag{2}$$

where TS_T and TS_B are the timestamps of the *Top SiPM* and *Bottom SiPM*, respectively.

In Method 2, the DOI-dependent time walk was corrected as follows[15]:

$$TS_{det} = W_T \times (TS_T - t_{relT}) + W_B \times (TS_B - t_{relB}) \tag{3}$$

where t_{relT} and t_{relB} are DOI-dependent time offsets found from the relationship between the relative timestamps and DOI index. The relative timestamps are calculated by subtracting the reference timestamp (TS_{Ref}) from the TS_T and TS_B. Weighting factors for SiPM's trigger times (W_T and W_B) are the normalized inverse variance factors (i.e., $W_T + W_B = 1$) and obtained as follows. First, the corrected relative timestamps ($t_{corrT,n}$ and $t_{corrB,n}$) are calculated at irradiation depth n mm (2, 6, 10, 14, 18 mm) as follows:

$$\begin{aligned} t_{corrT,n} &= TS_{T,n} - TS_{Ref,n} - t_{relT,n} \\ t_{corrB,n} &= TS_{B,n} - TS_{Ref,n} - t_{relB,n} \end{aligned} \tag{4}$$

where all data was obtained from side-on irradiation. Second, the variances of each depth, which are $V_{T,n}$ and $V_{B,n}$, were obtained by histogramming the corrected relative timestamps, and then normalized inverse of variances were calculated as follows:

$$NIV_{T,n} = \frac{1/V_{T,n}}{1/V_{T,n} + 1/V_{B,n}}, \quad NIV_{B,n} = \frac{1/V_{B,n}}{1/V_{T,n} + 1/V_{B,n}} \tag{5}$$

Last, the weighting factor was obtained by linear fitting the normalized inverse of variances at each depth as a function of the DOI index.

The coincidence timing resolution (CTR) of the proposed PET detector was then calculated as follows:

$$CTR_{det/det} = \sqrt{2} \cdot \sqrt{CTR^2_{det/ref} - STR^2_{ref}} \tag{6}$$

where $CTR_{det/ref}$ is the measured CTR value between the proposed PET detector and reference detector and STR_{ref} is the STR of the reference detector. We used only the coincidence events within the [350, 650] keV energy window surrounding the 511 keV photopeak. All timestamps were obtained by applying the digital constant fraction discriminator (CFD) method that reduces the time-walk effects. The trigger value, which is a constant fraction of the peak height of the time signal, was swept during CTR measurement to achieve optimal timing performance in our measurement setup. Inter-chip measurement was conducted to eliminate the high-frequency interference between adjacent DAQ channels within the DRS4 chip.[39]

3 | RESULTS

Figure 6 shows the DOI response for each crystal element of the proposed PET detector. Figure 6a shows the plots of the DOI indices, where each color represents five different DOI positions (2, 6, 10, 14, and 18 mm). All five DOI positions were well-resolved. The DOI resolution of the proposed detector was 2.2–2.9 mm depending on the crystal position (Figure 6b), and the average DOI resolution was 2.5 mm. Because the DOI resolution was measured by side-on irradiation as shown in Figure 4a, beam width was narrower, and more photopeak events occurred on the irradiation side, where DOI resolution is better than the opposite side.

The energy histograms and resolutions of each crystal element are shown in Figure 7. The average energy resolution of the proposed PET detector was 16% FWHM. The energy resolution of the center crystals was better than that of the edge crystals due to the higher light collection efficiency of the center crystals.

Figure 8a shows the photopeak values of the *Top SiPM* and *Bottom SiPM* in each crystal. The differences between each side's photopeak values indicate the necessity of the weighted average of the triggered times by considering the uncertainty of timing measurement depending on signal amplitude. In the optimization of the trigger value, the 7% and 5% amplitudes of the time signal yielded the best CTR values for Methods 1 and 2, respectively (Figure 8b).

The CTR of the proposed PET detector is shown in Figure 9. The average CTR was 448 ps FWHM using Method 1 and 411 ps FWHM using Method 2.

4 | DISCUSSIONS

A PET detector based on dual-ended signal readout provides continuous DOI information with excellent timing, energy, and DOI resolutions.[24–31] Therefore, it has been widely utilized in various high-resolution PET systems, particularly for small-animal and peripheral human organ imaging.[40–43] However, the increased material cost of the dual-ended signal readout scheme is a critical drawback since it requires twice the number of photosensors and readout electronics. To address the aforementioned issue, investigations on low-cost dual-ended readout PET detectors have been conducted. Zhang and Wong[28] explored a low-cost PET detector design (DO-QS) that utilized approximately half the number of SiPM elements relative to the number of scintillation crystals. In this configuration, it is possible to achieve uniform detector performance across the scintillation crystals because 25% of the crystal cross-section commonly touches the photosensors; however, a large portion of the non-contacted cross-section may lead to significant light loss. Additionally, the DO-QS method has not yet demonstrated its performance via real experiments. Another investigation for reducing the cost of PET system[29] is the DS-PS3 detector, which collects visible photons from a 15 × 15 array of 2-mm crystals using only 16 SiPM elements. However, the high degree of sparsity of the DS-PS3 detectors led to suboptimal performance in terms of energy resolution and crystal identification.

The PET detector proposed in this study has the advantage of simplicity in crystal identification despite the sparse SiPM arrangement because crystals can be easily identified by searching for a pair of *Active Top SiPM* and *Active Bottom SiPM* based on the look-up table. Our proposed method shows the energy resolution of 16% FWHM with a standard deviation of 1.6%, which is similar to DS-PS3 (16.6%) and DO-QS (16%, simulation data). Compared to DS-PS3 (3.6 mm), better

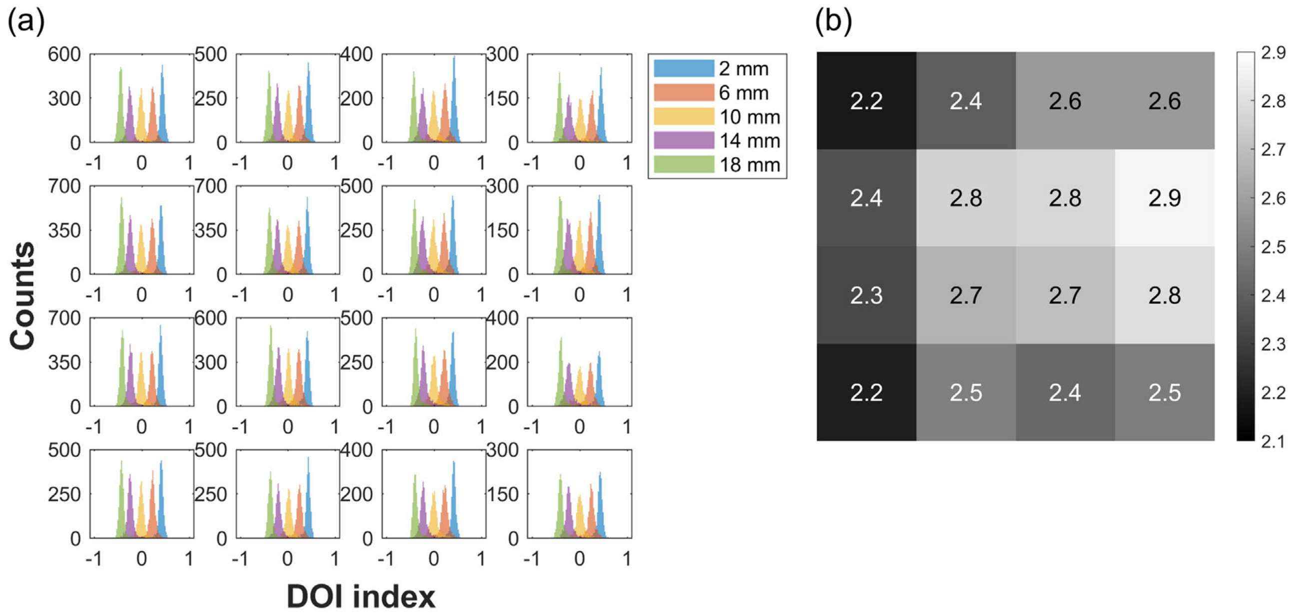

FIGURE 6 The DOI response of the proposed PET detector for each crystal. (a) DOI index at each DOI position, (b) DOI resolution.

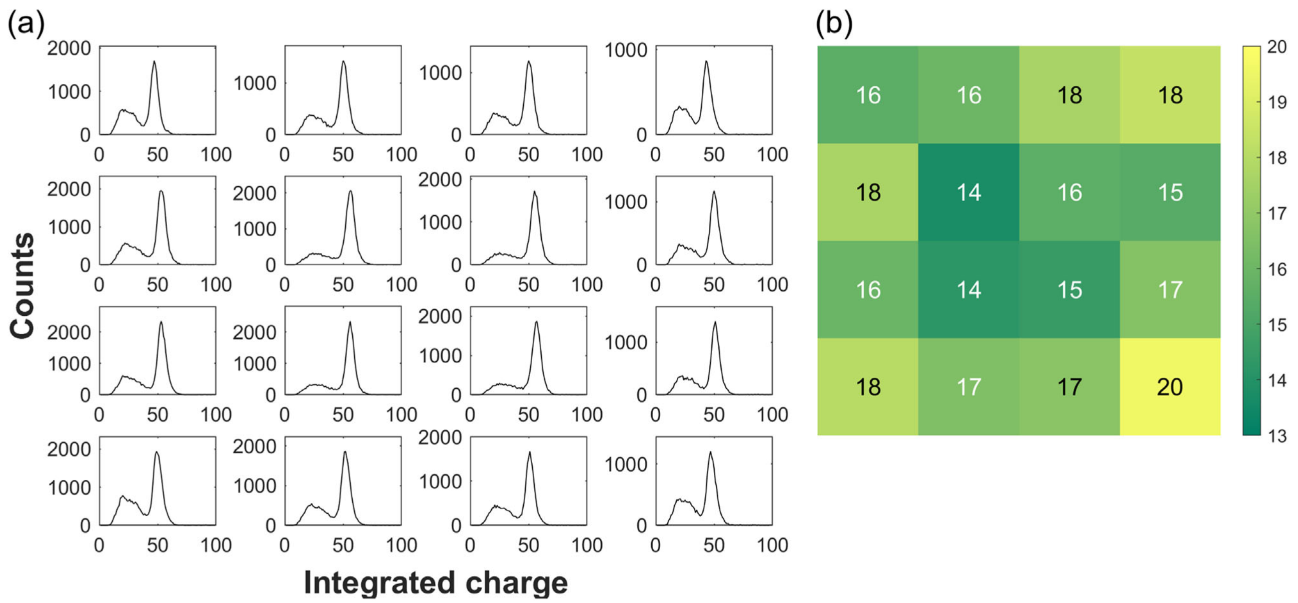

FIGURE 7 (a) The energy histogram and (b) the energy resolution of the proposed PET detector for each crystal.

DOI resolution was obtained using our method, probably due to the smaller SiPM sparsity. The timing resolution of our detector was 411 ps FWHM using Method 2, but the timing resolution of DS-PS3 and DO-QS is not available in the literature.

The DOI information obtained using the proposed detector improved the timing resolution from 448 ps FWHM (Method 1) to 411 ps FWHM by correcting the time walk due to annihilation and optical photon travel within the scintillation crystal. In Method 1, the timestamps of the *Top SiPM* and *Bottom SiPM* were averaged without using the measured DOI information. This method compensates for the optical photon transit time but does not correct the DOI-dependent transit time difference of annihilation photons.[15] In contrast, Method 2 improved the coincidence timing resolution by approximately 40 ps. This is because this method further compensates the DOI-dependent transit time difference of annihilation photons and considers the timing measurement uncertainty determined by optical photon statistics. The trigger value of CFD was also optimized to yield better timing resolution.

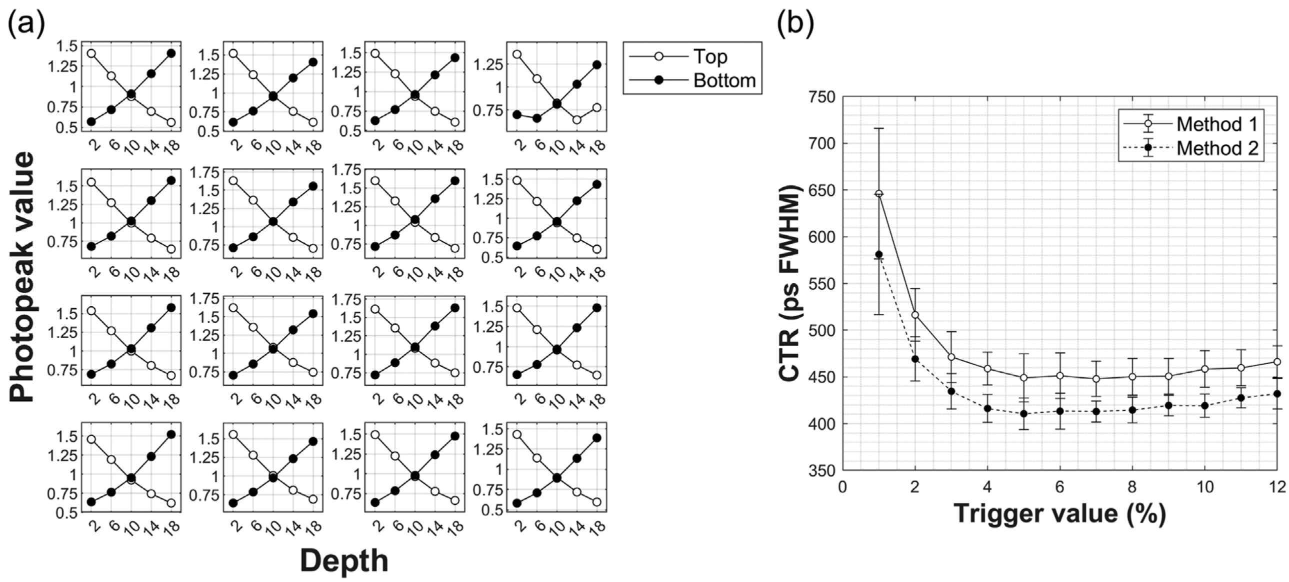

FIGURE 8 (a) Each crystal's photopeak values in the *Top SiPM* and *Bottom SiPM* at five different DOI positions. (b) Average CTR value of the proposed PET detector as a function of the trigger value.

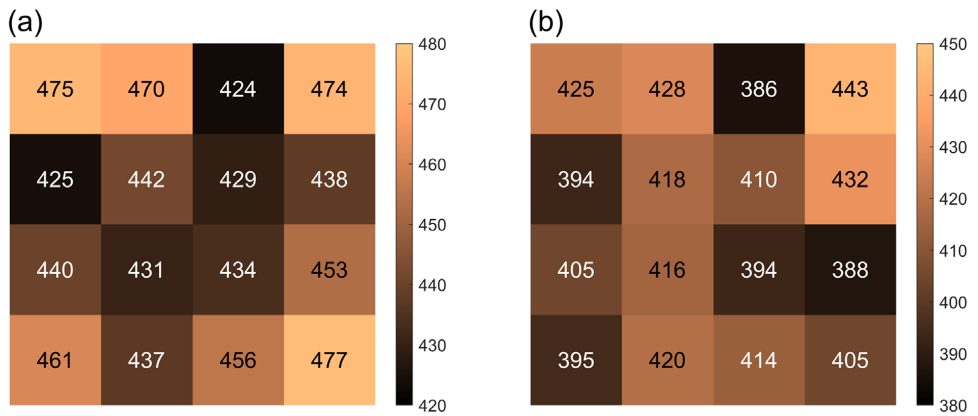

FIGURE 9 The CTR value of the proposed PET detector in each crystal. (a) Method 1, (b) Method 2.

To look for the impact of our 45° tilted SiPM arrangement, we compared our detector with several detector configurations. Kang *et al.*[25] explored the one-to-one coupled PET detector based on single- and dual-ended readouts with various crystal surface treatments. Among the various detector configuration, the detector that featured similar crystal conditions achieved the best DOI value (2.2 mm) with 10.6% (before correcting the SiPM saturation effect) energy resolution and 291 ps CTR value. The better energy and timing resolution of this detector than our detector owed to simple one-to-one coupling minimizing light collection loss and readout electronics noise. Liu *et al.*[30] tested with similar crystal conditions to our condition for whole-body PET application without using sparse SiPM configurations. The DOI and energy resolution of this detector were 3.5 mm and 10.2% while the timing resolution of this detector was 180 ps with ultrafast NINO application-specific integrated circuit (ASIC),[44] which is better than our detector timing performance (411 ps). Even though the timing resolution of our design is not enough for the time-of-flight (TOF) PET application, our design provides great DOI resolution and reasonable energy resolution for an organ-dedicated PET system.[45] For example, Kuang et al.[46] explored a dual-ended readout detector for a brain PET scanner, yielding good DOI and energy resolution (2.33 mm and 16.1%) and poor timing resolution (1.6 ns). Also, the additional reflector or light guide on the non-contacted cross-section of the crystal array can reduce the light collection loss.

This study has some limitations. First, only a single PET detector sample consisting of an LSO array was tested to demonstrate the feasibility of the proposed method. Further investigation using various types and sizes of scintillation crystals and SiPMs will increase the reliability of the proposed method.[25,47] Second, we did not measure the count rate performance since our experimental setup based on the DRS4 digitizer was unsuitable for evaluating the count rate performance. The count rate performance of the proposed method is expected to be worse than that of other PET detectors based on the one-to-one coupling of crystals and SiPMs but better than that of other light-sharing detectors. Third, the timing resolution obtained with our method is poor compared to state-of-the-art clinical PET detectors without DOI measurement capability, mainly due to light collection loss. All polished crystals can improve timing performance; however, they can degrade DOI performance.[25] Fourth, in our detector design, photodetectors extend beyond crystals. This will widen the spacing between the detectors when constructing detector rings. However, for clinical-scale PET systems employing larger detectors with more crystal and SiPM elements, the extended spacing may not be significant compared to the detector size. Last, the validity of the proposed method was evaluated at the detector level, and not at the PET system level.

5 | CONCLUSIONS

In this study, we proposed a novel cost-effective PET detector using sparsely arranged SiPMs tilted by 45°. Our novel PET detector design will be useful for the development of cost-effective high-resolution PET systems.

ACKNOWLEDGEMENTS

This work was supported by the Korea Medical Device Development Fund grant funded by the Korean government (Ministry of Science and ICT, Ministry of Trade, Industry and Energy, Ministry of Health & Welfare, Ministry of Food and Drug Safety) (Project Nos. 1711137868 and RS-2020-KD000006), and grants from the National Research Foundation of Korea (NRF) funded by the Korean Ministry of Science and ICT (grant number 2020M2D9A1093989) and Ministry of Education (grant number 2018R1D1A1B07045559).

CONFLICT OF INTEREST STATEMENT

The authors have no relevant conflicts of interest to disclose.

REFERENCES

1. Peng F. Recent advances in cancer imaging with 64 CuCl 2 PET/CT. *Nucl Med Mol Imaging*. 2022;56(2):80-85.
2. Leroy-Freschini B, Lindner V, Boisramé T, Demarchi M. 18 F-FDG PET/CT imaging of peritoneal fibrosis mimicking persistent metastatic ovarian carcinoma. *Nucl Med Mol Imaging*. 2020;54(5):249-251.
3. Siripongsatian D, Promteangtrong C, Kunawudhi A, Kiatkittikul P, Chotipanich C. 68 Ga-FAPI-46 PET/MR detects recurrent cholangiocarcinoma and intraductal papillary mucinous neoplasm in a patient showing increasing CEA with negative 18 F-FDG PET/CT and conventional CT. *Nucl Med Mol Imaging*. 2021;55(5):257-260.
4. Chatziioannou AF. Molecular imaging of small animals with dedicated PET tomographs. *Eur J Nucl Med Mol Imaging*. 2002;29(1):98-114.
5. MG P, JS L. Small animal imaging in drug development. *Curr Pharm Des*. 2005;11(25):3247-3272.
6. Xi W, Tian M, Zhang H. Molecular imaging in neuroscience research with small-animal PET in rodents. *Neurosci Res*. 2011;70(2):133-143.
7. González AJ, Sánchez F, Benlloch JM. Organ-dedicated molecular imaging systems. *IEEE Trans Radiat Plasma Med Sci*. 2018;2(5):388-403.
8. Catana C. Development of dedicated brain PET imaging devices: recent advances and future perspectives. *J Nucl Med*. 2019;60(8):1044-1052.
9. Nakamoto R, Nakamoto Y, Ishimori T, et al. Diagnostic performance of a novel dedicated breast PET scanner with C-shaped ring detectors. *Nucl Med Commun*. 2017;38(5):388-395.
10. García Hernández T, Vicedo González A, Ferrer Rebolleda J, et al. Performance evaluation of a high resolution dedicated breast PET scanner. *Med Phys*. 2016;43(5):2261-2272.
11. Raylman RR, van Kampen W, Stolin AV, et al. A dedicated breast-PET/CT scanner: evaluation of basic performance characteristics. *Med Phys*. 2018;45(4):1603-1613.
12. Yoshida E, Tashima H, Akamatsu G, et al. 245 ps-TOF brain-dedicated PET prototype with a hemispherical detector arrangement. *Phys Med Biol*. 2020;65(14):145008.
13. Won JY, Park H, Lee S, et al. Development and initial results of a brain PET insert for simultaneous 7-Tesla PET/MRI using an FPGA-only signal digitization method. *IEEE Trans Med Imaging*. 2021;40(6):1579-1590.
14. Ito M, Hong SJ, Lee JS. Positron emission tomography (PET) detectors with depth-of- interaction (DOI) capability. *Biomed Eng Lett*. 2011;1(2):70-81.
15. Guo L, Tian J, Chen P, Derenzo SE, Choong WS. Improving timing performance of double-ended readout in TOF-PET detectors. *J Instrum*. 2020;15(01):P01003-P01003.
16. Spanoudaki VC, Levin CS. Investigating the temporal resolution limits of scintillation detection from pixellated elements: comparison between experiment and simulation. *Phys Med Biol*. 2011;56(3):735-756.
17. Hong SJ, Kwon SI, Ito M, et al. Concept verification of three-layer DOI detectors for small animal PET. *IEEE Trans Nucl Sci*. 2008;55(3):912-917.
18. Prout DL, Gu Z, Shustef M, Chatziioannou AF. A digital phoswich detector using time-over-threshold for depth of interaction in PET. *Phys Med Biol*. 2020;65(24):245017.
19. Watanabe M, Saito A, Isobe T, et al. Performance evaluation of a high-resolution brain PET scanner using four-layer MPPC DOI detectors. *Phys Med Biol*. 2017;62(17):7148.
20. Akamatsu G, Tashima H, Iwao Y, et al. Performance evaluation of a whole-body prototype PET scanner with four-layer DOI detectors. *Phys Med Biol*. 2019;64(9):095014.
21. Ito M, Lee MS, Lee JS. Continuous depth-of-interaction measurement in a single-layer pixelated crystal array using a single-ended readout. *Phys Med Biol*. 2013;58(5):1269-1282.
22. Pizzichemi M, Polesel A, Stringhini G, et al. On light sharing TOF-PET modules with depth of interaction and 157 ps FWHM coincidence time resolution. *Phys Med Biol*. 2019;64(15):155008.
23. Mueller F, Naunheim S, Kuhl Y, Schug D, Solf T, Schulz V, A semi-monolithic detector providing intrinsic DOI-encoding and sub-200 ps CRT TOF-capabilities for clinical PET applications. Published online 2022.
24. Du J, Ariño-Estrada G, Bai X, Cherry SR. Performance comparison of dual-ended readout depth-encoding PET detectors based on BGO and LYSO crystals. *Phys Med Biol*. 2020;65(23).

25. Kang HG, Yamaya T, Han YB, et al. Crystal surface and reflector optimization for the SiPM-based dual-ended readout TOF-DOI PET detector. *Biomed Phys Eng Express*. 2020;6(6):065028.
26. Kang HG, Ko GB, Rhee JT, Kim KM, Lee JS, Hong SJ. A dual-ended readout detector using a meantime method for SiPM TOF-DOI PET. *IEEE Trans Nucl Sci*. 2015;62(5):1935-1943.
27. Kwon SI, Roncali E, Gola A, Paternoster G, Piemonte C, Cherry SR. Dual-ended readout of bismuth germanate to improve timing resolution in time-of-flight PET. *Phys Med Biol*. 2019;64(10):105007.
28. Zhang Y, Wong WH, Design study of a practical-entire-torso PET (PET-PET) with low-cost detector designs. *2016 IEEE Nuclear Science Symposium, Medical Imaging Conference and Room-Temperature Semiconductor Detector Workshop, NSS/MIC/RTSD 2016*. 2017;2017-January.
29. Hunter WCJ, de Witt DQ, Miyaoka RS. Performance characteristics of a dual-sided position-sensitive sparse-sensor detector for gamma-ray imaging. *IEEE Trans Radiat Plasma Med Sci*. 2021;7311(c):1-1.
30. Liu Z, Niu M, Kuang Z, et al. High resolution detectors for whole-body PET scanners by using dual-ended readout. *EJNMMI Phys*. 2022;9(1):29.
31. Du J. Performance of dual-ended readout PET detectors based on BGO arrays and BaSO reflector. *IEEE Trans Radiat Plasma Med Sci*. 2022;6(5):522-528.
32. Lee MS, Lee JS. Depth-of-interaction measurement in a single-layer crystal array with a single-ended readout using digital silicon photomultiplier. *Phys Med Biol*. 2015;60(16):6495-6514.
33. Yoshida E, Obata F, Kamada K, Yamaya T. A crosshair light sharing PET detector with DOI and TOF capabilities using four-to-one coupling and single-ended readout. *IEEE Trans Radiat Plasma Med Sci*. 2021;5(5):638-644.
34. Ito M, Lee JS, Kwon SI, et al. A four-layer DOI detector with a relative offset for use in an animal PET system. *IEEE Trans Nucl Sci*. 2010;57(3 PART 1):976-981.
35. Roncali E, Viswanath V, Cherry SR. Design considerations for DOI-encoding PET detectors using phosphor-coated crystals. *IEEE Trans Nucl Sci*. 2014;61(1):67-73.
36. Kang HG, Nishikido F, Yamaya T. A staggered 3-layer DOI PET detector using BaSO4 reflector for enhanced crystal identification and inter-crystal scattering event discrimination capability. *Biomed Phys Eng Express*. 2021;7(3).
37. Sumanasena MGB, Peng Q, Godinez F, et al. A prototype PET scanner with hybrid DOI-encoding detectors. *2015 IEEE Nuclear Science Symposium and Medical Imaging Conference, NSS/MIC 2015*. Published online October 3, 2016.
38. Yang Y, Dokhale PA, Silverman RW, et al. Depth of interaction resolution measurements for a high resolution PET detector using position sensitive avalanche photodiodes. *Phys Med Biol*. 2006;51(9):2131-2142.
39. Park H, Lee S, Ko GB, Lee JS. Achieving reliable coincidence resolving time measurement of PET detectors using multichannel waveform digitizer based on DRS4 chip. *Phys Med Biol*. 2018;63(24):24NT02.
40. Kuang Z, Wang X, Ren N, et al. Design and performance of SIAT aPET: a uniform high-resolution small animal PET scanner using dual-ended readout detectors. *Phys Med Biol*. 2020;65(23):235013.
41. Mohammadi A, Inadama N, Nishikido F, Yamaya T. Development of dual-ended depth-of-interaction detectors using laser-induced crystals for small animal PET systems. *Phys Med Biol*. 2021;66(17).
42. Godinez F, Chaudhari AJ, Yang Y, Farrell R, Badawi RD. Characterization of a high-resolution hybrid DOI detector for a dedicated breast PET/CT scanner. *Phys Med Biol*. 2012;57(11):3435-3449.
43. Lai Y, Wang Q, Zhou S, et al. H 2 RSPET: a 0.5 mm resolution high-sensitivity small-animal PET scanner, a simulation study. *Phys Med Biol*. 2021;66(6):065016.
44. Anghinolfi F, Jarron P, Krummenacher F, Usenko E, Williams MCS. NINO: an ultrafast low-power front-end amplifier discriminator for the time-of-flight detector in the ALICE experiment. *IEEE Trans Nucl Sci*. 2004;51(5I):1974-1978.
45. Kuang Z, Sang Z, Wang X, et al. Progress of SIAT bPET: an MRI compatible brain PET scanner with high spatial resolution and high sensitivity. *J Nucl Med*. 2022;63:2437-2437. supplement 2.
46. Kuang Z, Sang Z, Wang X, et al. Design and development of an MRI compatible human brain PET scanner by using dual-ended readout detectors. *J Nucl Med*. 2021;62:1708. supplement 1.
47. Ren S, Yang Y, Cherry SR. Effects of reflector and crystal surface on the performance of a depth-encoding PET detector with dual-ended readout. *Med Phys*. 2014;41(7):072503.

How to cite this article: Seo M, Park H, Lee S, Ko GB, Lee JS. Depth-of-interaction positron emission tomography detector with 45° tilted silicon photomultipliers using dual-ended signal readout. *Med Phys*. 2023;50:4112–4121. https://doi.org/10.1002/mp.16355